Synthesis of Fly Ash-Based Geopolymers: Effect of Calcite Addition and Mechanical Activation

Alexander M. Kalinkin [1,*], **Basya I. Gurevich** [1], **Mikhail S. Myshenkov** [2],
Mikhail V. Chislov [2], **Elena V. Kalinkina** [1], **Irina A. Zvereva** [2], **Zara Cherkezova-Zheleva** [3],
Daniela Paneva [3] and **Vilma Petkova** [4]

1   Tananaev Institute of Chemistry—Subdivision of the Federal Research Centre "Kola Science Centre of the Russian Academy of Sciences", Apatity 184209, Murmansk Region, Russia; gurevich1931@yandex.ru (B.I.G.); e.kalinkina@ksc.ru (E.V.K.)
2   Centre for Thermogravimetric and Calorimetric Research, Saint Petersburg State University, St. Petersburg 199034, Russia; m.myshenkov@spbu.ru (M.S.M.); mikhail.chislov@spbu.ru (M.V.C.); irina.zvereva@spbu.ru (I.A.Z.)
3   Institute of Catalysis, Bulgarian Academy of Sciences, 1113 Sofia, Bulgaria; zzhel@ic.bas.bg (Z.C.-Z.); daniela@ic.bas.bg (D.P.)
4   Institute of Mineralogy and Crystallography, Bulgarian Academy of Sciences, 1113 Sofia, Bulgaria; vpetkova@clmc.bas.bg
*   Correspondence: a.kalinkin@ksc.ru; Tel.: +7-81555-79523

Abstract: Blends of fly ash and natural calcite, mechanically activated for 0–400 s in a planetary mill, were used to synthesize geopolymers at ambient temperature. The calcite content in the blends was 0–10 wt.%. Sodium hydroxide solution was used as an alkaline agent. Mechanical activation of the raw material considerably enhanced its reactivity with respect to the alkaline agent, as was observed using Fourier-transform infrared spectroscopy, isothermal conduction calorimetry, thermogravimetry coupled with mass spectrometry analysis of the evolved gas, and SEM/EDS. The addition of calcite to the fly ash improved the compressive strength of the geopolymers, especially during the early age of curing. For 7 d aged geopolymers based on the 90% fly ash + 10% calcite blend, the strength was 8.0-, 3.5- and 2.9-fold higher than that for the geopolymers based on the unblended fly ash for 30 s, 180 s and 400 s mechanical activation time, respectively. Using Mössbauer spectroscopy, it was revealed that iron present in the fly ash did not play a significant part in the geopolymerization process. The dominant reaction product was sodium containing aluminosilicate hydrogel (N-A-S-H gel). Calcite was found to transform, to a small extent, to vaterite and $Ca(OH)_2$ in the course of the geopolymerization.

Keywords: fly ash; natural calcite; mechanical activation; geopolymers

1. Introduction

Despite the intensive development of nuclear energy from the middle of the 20th century, the contribution of coal to the total generated global energy remains very large and amounts to about 40% [1]. The combustion of the carbonaceous part of coal in power plants occurs at high temperatures of about 1500 °C and a heating rate of 10^6 deg/s [2]. As a result of very complex processes, the mineral part of coal thermally decomposes and melts in the combustion flame to generate the solid powdered residue in the form of fly ash and bottom ash. The fly ash (85–95 wt.% of the total ash) consists of fine particles which are collected by electrostatic precipitation, or mechanical capture, from the flue gas, while the coarser bottom ash falls through the air stream to the bottom of the boiler and is removed mechanically [3]. The mineral composition of coal ash is represented mainly by the glass phase, similar

to volcanic glass, as well as by quartz, mullite, magnetite, etc. The total annual worldwide coal ash generation is 700–800 million tons, with less than 30% being reused [3,4]. The disposed coal ash has become a matter of serious environmental concern because of its heavy metal contents which may leach out causing serious pollution of natural water bodies and soil [5].

Among the large number of proposed options for the utilization of coal ash [1,3], the main one is the construction industry. High-calcium fly ash (Class C) can be used as a binder due to its considerable cementitious properties, and low-calcium fly ash (Class F) has pozzolanic activity and is utilized as a blend with Portland cement. In recent years, intensive research has been carried out in the use of Class F fly ash for the synthesis of geopolymer materials. Geopolymers, also referred to as inorganic polymers, are a subclass of alkali activated materials prepared by the reaction of low-calcium, natural and industrially produced aluminosilicates, with an alkaline agent (e.g., alkali metal hydroxide solution or liquid glass) at near ambient temperatures [6–10]. Because of energy saving, environmentally benign processing, and high performance, geopolymers have received attention in construction engineering as a promising substitute to traditional Portland cement. Besides, due to their thermal and fire resistance [11,12], chemical stability [13,14], stability under irradiation [15], and ion-exchange capacity [16,17], geopolymer materials can be potentially used in such applications as refractories and fireproof materials, heavy metal and radioactive waste immobilization, wastewater treatment, and many others [18–23].

The geopolymerization mechanism of fly ash is similar to that of metakaolin (anhydrous calcined form of the clay mineral kaolinite) [13,24]. Simplified, it can be represented in the form of conjoined reactions: (1) destruction/dissolution of the raw material; (2) formation of supersaturated aluminosilicate solution; (3) gelation (precipitation of sodium containing aluminosilicate hydrogel (N-A-S-H gel)); (4) restructuring of the gel; and (5) polymerization and hardening, resulting in a three-dimensional aluminosilicate network [25,26]. As a raw material for geopolymerization, fly ash is preferred for its easy accessibility, good workability, durability of the resultant geopolymers, and environmental reasons [27,28]. However, the reactivity of fly ash in geopolymer synthesis is relatively low [29]. The main factors affecting the reactivity of fly ash are the particle fineness and the amount and composition of the glass phase as the most reactive constituent of fly ash [24,30,31]. The reactivity of fly ash can be characterized using isothermal conduction calorimetry [32,33], Fourier-transform infrared (FTIR) spectroscopy [34], and other experimental and calculated techniques [35–37].

It has been reported in many publications that mechanical activation (MA) is an effective tool of enhancing the fly ash reactivity in the geopolymer synthesis [29,31,32,38–49]. MA in mills is a complex multi-stage process in which, from the point of view of influencing the reactivity of the solids, the following factors are important: (i) changes in the specific surface area (particle size); and (ii) the appearance and relaxation of various structural defects (point, linear, planar) [50–52]. At the initial stage, the effect of the milling is dominated mainly by particle size reduction (the Rittinger stage). Subsequently, the specific surface area of the powder, passing through the maximum, begins to decrease due to aggregation and agglomeration of particles. It is at this stage, when comminution slows down and stops, the processes of plastic deformation and generation of defects (importantly, "long-living" ones which do not disappear with quick relaxation [51]) are intensified due to the large number of contacts of the small particles [53,54]. The influence of these two factors on the reactivity of fly ash in geopolymerization reactions was recently shown by Kato et al. [47]. A comprehensive analysis of the effect of MA of different fly ashes using various type of mills and synthesis conditions on reaction, structure and properties of resulting geopolymers was presented by R. Kumar, S. Kumar et al. [29,32,38,39,45], Mucsí et al. [40,44,49], Temuujin et al. [42] and other researchers.

In recent years, the combination of aluminosilicate-rich materials (fly ash, metakaolin or other clay-based raw materials) with calcium carbonate containing mineral additives, such as limestone or dolomite, has received considerable attention for improving the mechanical, durability-related and other properties of alkali-activated binder systems [55–65]. It was revealed that adding a proper amount of limestone (<30%) to fly ash benefits the workability and the compressive strength, not

only due to the simple filler effect [55,59,61], but to a certain extent, through participation in the dissolution processes and geopolymer gel formation [57,60,62,63]. Moreover, it was shown that calcite and limestone themselves alkali activated with waterglass, displayed cementitious properties [60,66]. In this study, we focused on the effect of both calcium carbonate (in the form of natural calcite) addition to fly ash and MA of this two-component mixture on the geopolymerization process. The influence of calcite dosage and MA time on the reactivity of the raw material, with respect to the sodium hydroxide solution and the geopolymer strength, was investigated.

2. Materials and Methods

2.1. Materials

Class F fly ash (FA) was gathered from a thermal power plant located in Apatity, Murmansk Region, Russia. The Brunauer–Emmett–Teller (BET) and Blaine surface areas of the raw FA were 4.62 m^2/g and 230 m^2/kg, respectively. Particle-size distribution measurements showed that d_{90}, d_{50}, and d_{10} values of raw FA were 53.3, 14.6, and 3.8 μm, respectively. The main crystalline phases in the FA are quartz and mullite (Figure 1). In addition, hematite and magnetite are present in small amounts in the FA.
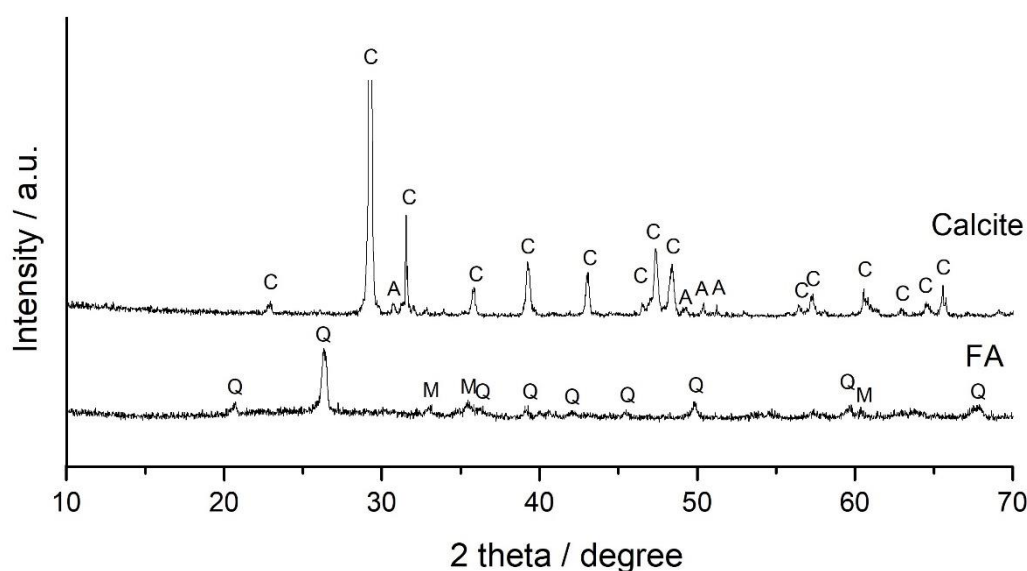

Figure 1. The X-ray diffraction patterns of the fly ash (FA) and natural calcite. Phases marked are: Q—quartz, M—mullite, C—calcite, A—augite.

Natural calcite (~98% $CaCO_3$) was taken from the calcite vein of carbonatite, an igneous rock in the Kovdor massif, Murmansk Region, Russia. Augite (Figure 1) and a minor amount of feldspar are present in calcite as admixtures. The calcite was ground in a ball mill and sieved with a 300 μm mesh. The chemical compositions of the FA and calcite are given in Table 1.

Table 1. Chemical composition of the FA and calcite, wt.%.

Raw Material	SiO_2	Al_2O_3	Fe_2O_3	FeO	CaO	MgO	SO_3	Na_2O	K_2O	C	P_2O_5	TiO_2	LOI *
FA	56.26	18.39	8.58	0.69	2.14	2.60	0.18	4.04	1.32	0.88	0.32	1.13	2.28
Calcite	0.24	0.47	0.67	-	52.1	1.44	0.15	1.76	0.56	-	0.05	0.05	43.0

* LOI: Loss on ignition.

2.2. Mechanical Activation

MA was carried out in an AGO-2 laboratory planetary mill (Novic, Novosibirsk, Russia) [53] at a centrifugal force of 40 g, in air, using steel vials and steel balls 8 mm in diameter as the milling bodies. The ratio of the mass of the balls to the mass of load was 6 (240 g of balls and 40 g of load in each vial). MA was carried out batchwise for periods of time ranging from 30 s to 400 s. For preparation of the geopolymers, FA + calcite mixtures milled for 30 s, 180 s, and 400 s were used. The parameters of MA were chosen based on previous work with the planetary mill [67,68]. In this paper, the terms "mechanical activation" ("MA") and "milling" refer to the same process of mechanical treatment using a planetary mill.

2.3. Preparation of Geopolymers

8.3 M NaOH solution was used as the alkaline agent. The mass ratio of Na_2O (present in sodium hydroxide solution) to the milled (FA + calcite) blends in the paste was equal to 0.06. The water content was adjusted to give the same workability of the pastes; therefore, the water content varied. The water to solid ratio (w/s) was defined considering the amount of water present in the NaOH solution. The composition of the mixtures used for preparation of the pastes are presented in Table 2. The unreacted (FA + calcite) blends are denoted as FAXC, where X is the calcite content in the blend, wt.%. The corresponding geopolymers, prepared using these blends, are denoted as GFAXC. The pastes were cast into 1.41 cm × 1.41 cm × 1.41 cm cubic molds. Prepared specimens were cured in a relative humidity of 95 ± 5% at 22 ± 2 °C for 24 h. After demolding, the specimens were further cured to testing time in the same conditions as applied in the first 24 h. Compressive strength data was obtained from an average of 3 samples after 7 and 28 days.

Table 2. Composition of mixtures used for preparation of pastes.

Mixture Code	FA (wt.%)	Calcite (wt.%)	NaOH (mol/L)	Na_2O/S Ratio	w/s Ratio (30 s MA)	w/s Ratio (180 s MA)	w/s Ratio (400 s MA)
FA0C	100	0	8.3	0.06	0.23	0.25	0.28
FA1C	99	1	8.3	0.06	0.23	0.22	0.25
FA3C	97	3	8.3	0.06	0.23	0.23	0.26
FA5C	95	5	8.3	0.06	0.23	0.23	0.26
FA10C	90	10	8.3	0.06	0.23	0.23	0.26

2.4. Characterization Methods

The specific surface area of the powders was measured using the standard Blaine test and nitrogen BET method with a Flow-Sorb II 2300 instrument (Micromeritics). The particle size distribution was determined using a SALD-201V (Shimadzu Corporation, Tokyo, Japan) laser diffraction particle size analyzer. Powder X-ray diffraction (XRD) patterns were recorded on a Shimadzu XRD-6000 (Shimadzu Corporation, Tokyo, Japan) instrument using Cu–K_α radiation. Scanning was carried out with a step of 0.02° (2 theta) and the dwell time was 1 s. FTIR spectra were recorded with a Nicolet 6700 (Thermo Electron Scientific Instruments Corporation, Madison, WI, USA) FTIR spectrometer using potassium bromide tablets. The morphologies of the hydration products were studied using a LEO 420 (Carl Zeiss, Jena, Germany) scanning electron microscope operated at 20 kV after gold coating on the fractured surface. Elemental analysis was done with an INCA Energy 400 (Oxford Instruments, Abington, UK) energy dispersive spectrometer (EDS) for X-ray microanalysis at the same voltage.

Calorimetric measurements were carried out using a TAM III (TA Instruments, New Castle, DE, USA) isothermal calorimeter at 25 °C. NaOH solution and milled powders were stored at 25 °C for 24 h until mixing. The powders were mixed with 6.5 M NaOH solution at the rate of 1 mL of solution per 3 g of powder. The prepared paste was placed in a 4-mL glass ampoule with a known mass, weighed, and immediately loaded into the calorimeter. The first 60 min were necessary for the system to achieve the thermal equilibrium, so the data recorded during this period was ignored. Thermogravimetric

(TG) analysis coupled with mass spectrometry (MS) was performed on a Netzsch STA 449F1 Phoenix coupled with a heated capillary column and a Netzsch QMS 402 Aeolos mass spectrometer (NETZSCH, Selb, Germany). Thermal analysis was performed at a heating rate of 20 °C/min under argon in platinum crucibles.

Mössbauer spectroscopy measurements were carried out on a Wissenschaftliche (Elektronic GmbH, Germany), operating in a constant acceleration mode (57Co/Rh source, α-Fe standard). The following parameters of hyperfine interactions of spectral components were determined by computer fitting: isomer shift (IS), quadrupole splitting (QS), effective hyperfine magnetic field (H_{eff}), line widths (FWHM), and component relative weights (G).

3. Results and Discussions

3.1. Effect of Mechanical Activation on the FA + Calcite Blends

Figure 2 shows the effect of MA on the Blaine-specific surface area (SSA) of the 100% FA (FA0C). During the Rittinger stage (0–180 s of MA), the Blaine SSA increases from 220 to 774 m²/kg. Then, because of aggregation of particles, the rate of the Blaine SSA increase gradually slows down. The Blaine SSA of FA milled for 400 s was 936 m²/kg, indicating that the SSA apparently reached a maximum between 300 and 400 s of MA. The BET SSA of the selected FA + CaCO₃ blends is also displayed in Figure 2. It can be seen that the addition of 1–10% of calcite to the FA only affects the SSA to a small extent.
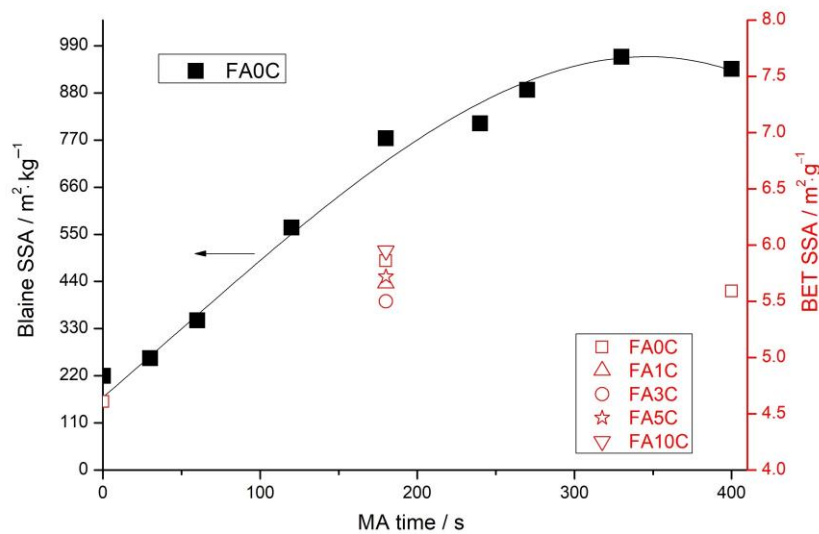

Figure 2. Blaine-specific surface area (SSA) of the fly ash (black symbols) and Brunauer–Emmett–Teller (BET) SSA of the FA + CaCO₃ blends milled for 180 s (red open symbols) vs. mechanical activation (MA) time.

Representative XRD patterns of the FA5C blend milled for 30 s and 180 s are shown in Figure 3. From comparison of the peak intensities, it is obvious that disorder of the mineral lattice and/or decrease of crystallite size induced by MA, for calcite, were noticeably more pronounced than those for quartz and mullite present in the FA. This can be explained by the difference in hardness of the minerals: for quartz, mullite, and calcite the hardness on the Mohs scale is 7, 6.3–7.5, and 3, respectively [69].
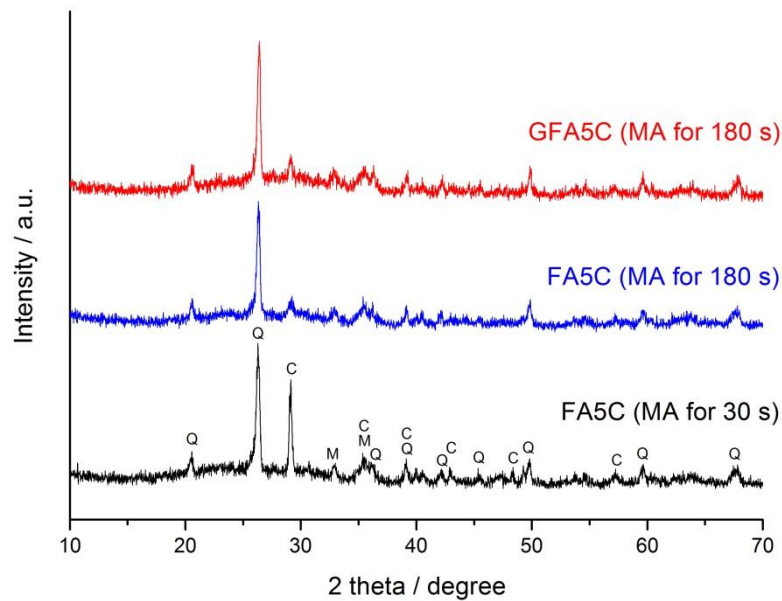
Figure 3. The X-ray diffraction patterns of the FA5C blend milled for 30 s and 180 s, and of the geopolymer prepared using the blend milled for 180 s after 28 d of curing (GFA5C). Phases marked are: Q—quartz, M—mullite, C—calcite.

3.2. Mechanical Properties

The results of the mechanical test measured after 7 and 28 days of curing are shown in Figures 4 and 5, respectively. For geopolymers based on the FA without calcite addition (GFA0C), the relatively low strength, which was within (0.5–7) MPa and (4–12) MPa in 7 and 28 d age, respectively, can be explained by the ambient curing temperature (22 ± 2 °C). Elevated curing temperatures favor the achievement of a higher strength of FA-based geopolymers [70,71]. However, for the purpose of comparative research, a model system of low strength is apparently more suitable for the further study of more complex systems [62].
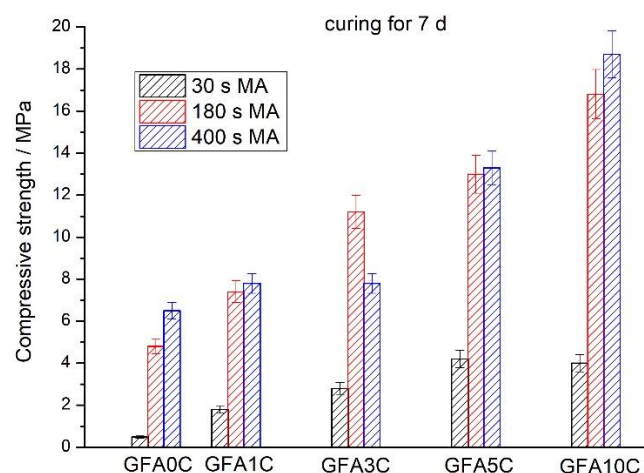

Figure 4. Effect of calcite content and MA time on the 7-day compressive strength of geopolymers.
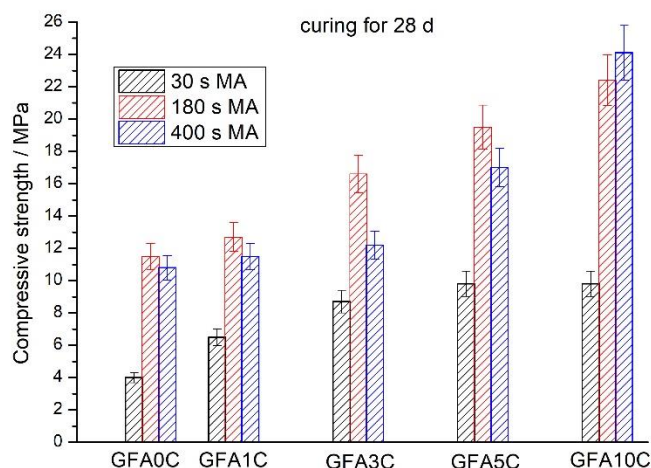
Figure 5. Effect of calcite content and MA time on the 28-day compressive strength of geopolymers.

Obviously, blending the FA with calcite results in an increase of strength with an increase in the proportion of $CaCO_3$ (Figures 4 and 5). The positive effect of calcite addition to the FA is more pronounced for the 7-d aged geopolymers. The GFA10C geopolymer after curing for 7 d shows a strength 8.0-, 3.5- and 2.9-fold higher than the GFA0C geopolymer for 30, 180 and 400 s milling time, respectively (Figure 4). In agreement with the SSA data (Figure 2), milling for 180 s in comparison to milling for 30 s results in a significant increase in strength. However, the effect of further milling from 180 to 400 s is either a very small positive or even deleterious (Figures 4 and 5). Although, as can be expected, the finer fly ash should display a better solubility in sodium hydroxide solution to produce a higher amount of geopolymer gel and, therefore, a higher strength. A similar effect of "overgrinding" on the compressive strength was observed for geopolymers based on fly ash milled using a ball mill, a vibratory mill, and a stirred media mill [44]. This was explained by the optimal particle size distribution which is another important factor affecting the mechanical properties of geopolymers. For workability reasons, the w/s ratio for geopolymers based on blends milled for 400 s was higher than that for mixtures milled for 180 s (Table 2). This can also lead to a decrease in the strength of the geopolymers based on the blends milled for 400 s. It is important to note that a further increase in both the MA time (>400 s) and the calcite content in the blends (>10%) led to a noticeable decrease in the workability of the pastes, the reasons for which are beyond the scope of this study. Thus, based on strength data and workability, the optimal MA time was 180 s.

3.3. Calorimetric and TG-MS Studies

Figure 6 displays the heat flow curves of the initial stages (within the first 24 h) of geopolymerization of the FA and its blends with calcite milled for 180 s. As is mentioned above, due to the nonequilibrium conditions, the calorimeter was not able to detect the information for the first 60 min of reaction. Because of this, an initial intensive exothermic peak was not fully recorded. Generally, for the alkali-activated fly ash or metakaolin without additives, this peak is associated with wetting and partial dissolution of the raw materials [39,72]. Blending with a moderate amount of calcium-containing material (blast furnace slag, $Ca(OH)_2$, $CaCO_3$) can accelerate geopolymerization reactions by the enhanced precipitation of the initial reaction products, simultaneously, with the dissolution stage [60,72–74]. Particularly, calcium carbonate might act as nucleation sites for the formation of reaction products [62,75]. Therefore, for the pastes prepared using the blends, the first heat flow peak may also be related to the precipitation of the initial reaction products. Within 0–5% calcite content in the blends, the heat flow curves are similar in shape: following the initial peak and short induction period, an acceleration period comes (Figure 6). In contrast to these blends, in the case of the FA10C blend (10% calcite), after the induction period (partially located within the first 60 min of reaction which was not recorded by the calorimeter) a second exothermic peak (acceleration and

deceleration) located at ~1.2 h appears. This peak is associated with the massive formation of the reaction products [72,75,76].
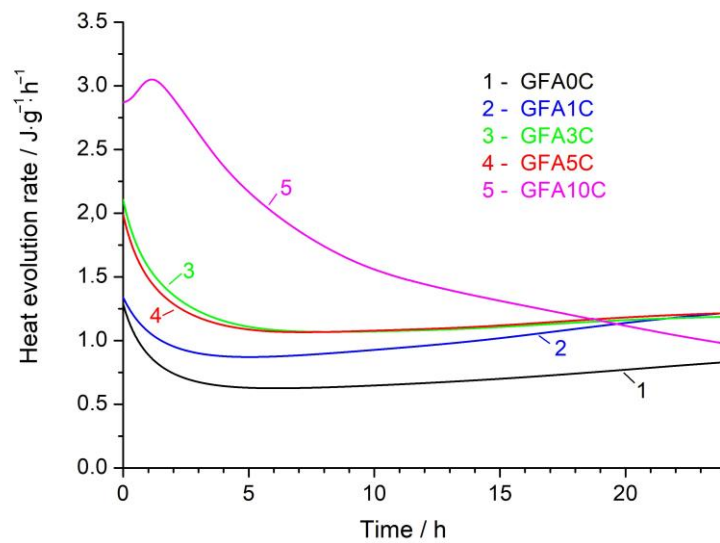

Figure 6. Heat flow curves of the initial stages of geopolymerization of the 100% FA and FA + calcite blends mechanically activated for 180 s.

Full time scale heat flow curves (Figure 7) show that the second calorimetry peak for the pastes prepared using the blends containing 0–5% calcite (GFA0C-GFA5C) is located at the 1.0–1.6 d range, which is notably later than that for the GFA10C paste (Figure 6). One of the reasons for this may be the highest ratio of NaOH solution/FA in the GFA10C paste compared to the other pastes. The influence of calcite and secondary Ca-containing phases identified in the GFA10C geopolymer is discussed below.
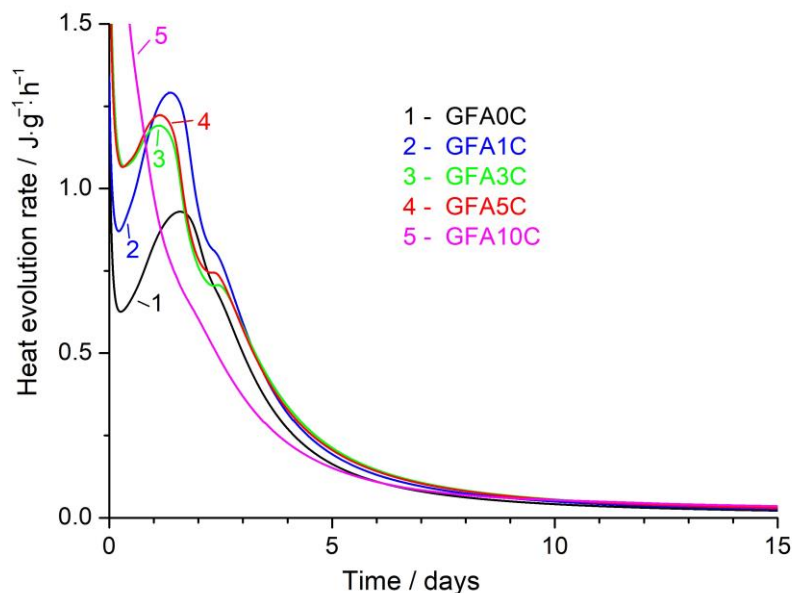

Figure 7. Full-time heat flow curves of geopolymerization of the 100% FA and FA + calcite blends mechanically activated for 180 s.

As the calcite content increases, the position of the second calorimetry peak shifts to earlier locations, indicating acceleration of the alkali-activated reaction process in the presence of calcite. This agrees with the geopolymer strengths trend (Figure 4). Before the deceleration stage, a smaller,

third exothermic peak at ~2.4 d appears for the GFA0C-GFA5C pastes related to the further precipitation of the reaction products.

Figure 8 displays thermogravimetric (TG) curves of the geopolymers based on the FA without additives and the blends milled for 180 s in the 28-d age. The weight loss before about 300 °C is associated with dehydration—removal of free and relatively loosely bound water from the N-A-S-H gel. In the differential thermogravimetric (DTG) curves of all specimens, this stage is consistent with the peak at ~122 °C (Figure 9). With an increase in temperature above 300 °C, elimination of water occurs mainly by condensation of the silanol or aluminol groups of the geopolymeric gel [77,78]. As hydroxyl groups are slowly removed over a rather wide temperature region [77], this stage may not be evident in the DTG curves (Figure 9). With a further increase in temperature, the weight loss is related to the decomposition of carbonates (Figure 8).
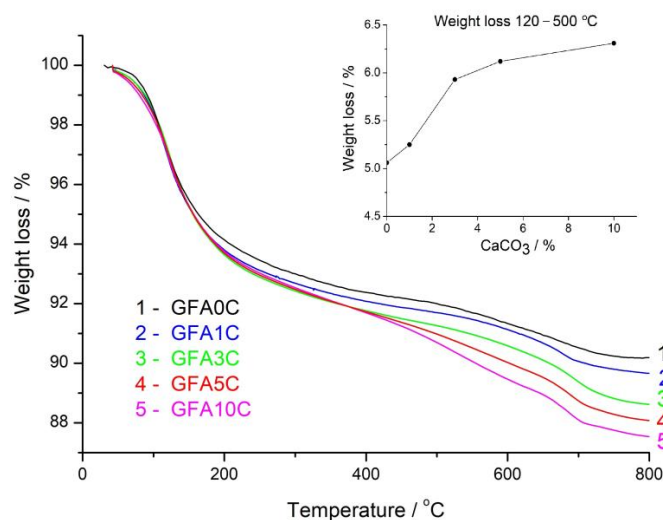

Figure 8. Thermogravimetric (TG) curves of the geopolymers based on the 100% FA (GFA0C) and the FA + calcite blends (GFA1C-GFA10C) mechanically activated for 180 s and cured for 28 d. In the insert, the weight loss of the geopolymers in 120–500 °C temperature range vs. calcium carbonate content in the blends is shown.
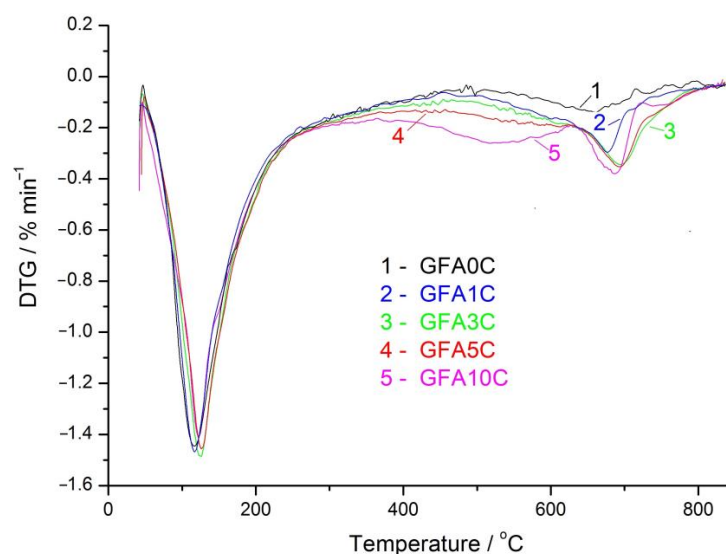

Figure 9. Differential thermogravimetric (DTG) curves of geopolymers based on the 100% FA and FA + calcite blends mechanically activated for 180 s and cured for 28 d.

MS analysis of the evolved gas (Figure 10) shows that removal of water occurs up to about 500 °C, while at higher temperatures decarbonization is mainly observed. If we assume that the water tightly bound with N-A-S-H gel (in molecular and hydroxyl forms) is removed after 120 °C, then the weight loss between the 120 and 500 °C temperature range can be considered as a measure of the geopolymer gel formation. From the insert in Figure 8, it is obvious that the addition of calcite to the FA accelerates the formation of the geopolymer gel which agrees with the mechanical properties (Figure 5) and the isothermal conduction calorimetry results (Figures 6 and 7).
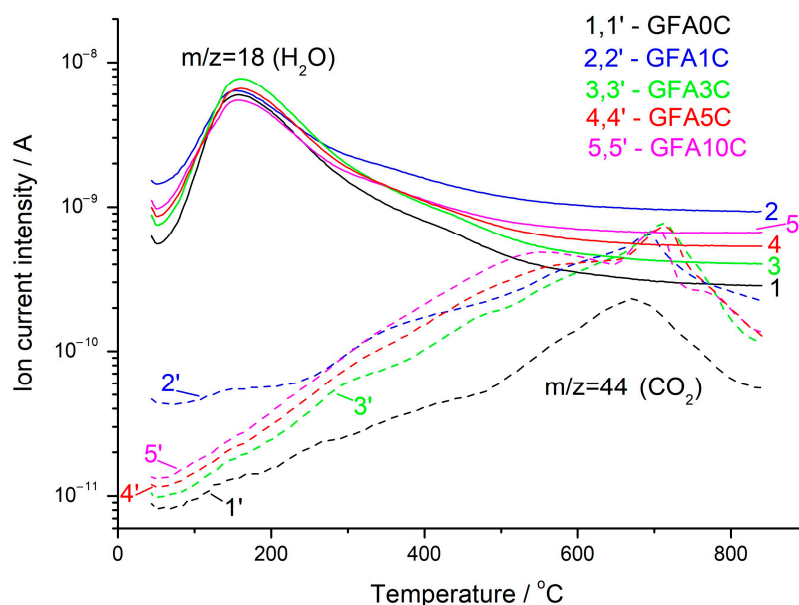

Figure 10. Ion current of the collected gas, $m/z = 18(H_2O)$ (solid lines) and $m/z = 44(CO_2)$ (dashed lines) for the geopolymers based on the 100% FA and FA + calcite blends mechanically activated for 180 s and cured for 28 d.

Coherent with the MS data of the collected gas (Figure 10), the DTG curves for GFA0C-GFA5C geopolymers show one main peak in the 450–800 °C region, related to decarbonization (Figure 9). For the geopolymer based on 100% FA (FA0C), this peak, centered at about 660 °C, is relatively weak and can be attributed to decomposition of sodium carbonates formed due to the interaction of the alkaline agent with atmospheric CO_2 [79]. For the geopolymers prepared using the blends, the main decarbonization peak is related to the decomposition of calcite [62]. It is remarkable that, as in the case of the heat flow curves (Figures 6 and 7), the DTG curve for the GFA10C differs from the curves of the other geopolymers. The main difference is that the GFA10C specimen shows another DTG decarbonization peak centered at 540 °C (Figure 9). In addition, the intensity of the peak of calcite decomposition for GFA10C, at about 690 °C, is comparable to the intensities of the peaks for GFA3C and GFA2C, although the content of calcium carbonate in the former is several times higher than in the latter. This indicates the partial transformation of calcite into another, less stable carbonate phase. The DTG peak width of this phase at 540 °C may indicate its low crystallinity.

Bernal et al. [79] revealed that accelerated carbonation of fly ash/slag alkali binder in a CO_2-rich atmosphere resulted in the formation of vaterite, a polymorph of $CaCO_3$, which displayed a DTG peak of decomposition at about 550 °C. It can be assumed that in our case, calcite transformed into vaterite. It is also possible that the DTG peak at 540 °C corresponds to decarbonization of a geopolymerization reaction product of unknown composition.

3.4. XRD and FTIR Spectroscopy Analysis

As a representative example of the geopolymers prepared using the blends containing 5% $CaCO_3$ or less, Figure 3 shows the XRD pattern of the GFA5C specimen (MA for 180 s, curing for 28 d). No new peaks of crystalline phases are seen in the diffractogram and the peak intensities seem to be unchanged in comparison to those in the XRD pattern of the FA5C blend. Therefore, the product of geopolymerization (N-A-S-H gel) is X-ray amorphous. Its formation is confirmed by the appearance of a halo in the $2\theta = 25$–$35°$ region. This agrees with previous works in which near ambient temperature curing conditions were employed to prepare geopolymers based on fly ash [45,80].

Again, in line with calorimetric results (Figures 6 and 7) and DTG data (Figure 9), the GFA10C specimen stands out from the series of geopolymers studied. Unlike geopolymers based on the blends containing less calcite, the XRD pattern of the GFA10C displays small peaks which can be attributed to a newly formed phase—vaterite (PDF 33-268), a $CaCO_3$ polymorph (Figure 11). Along with this, the main calcite reflection, at about $2\theta = 29.4°$ in the XRD pattern of the GFA10C, slightly decreased in intensity relative to that of the FA10C blend (Figure 11). This supports the transformation of calcite into vaterite based on DTG data (Figure 9). This transformation can proceed through recrystallization in NaOH solution following the Ostwald step rule [79,81]. The solubility of $CaCO_3$ (calcite) in sodium hydroxide solution is low (less than 1 mM in 1 M NaOH at 25 °C [62,82]). However, MA of calcite in a planetary mill results in the considerable reduction of particle size and accumulation of structural defects, as supported by the XRD data (Figure 3), which should increase its solubility to some extent.
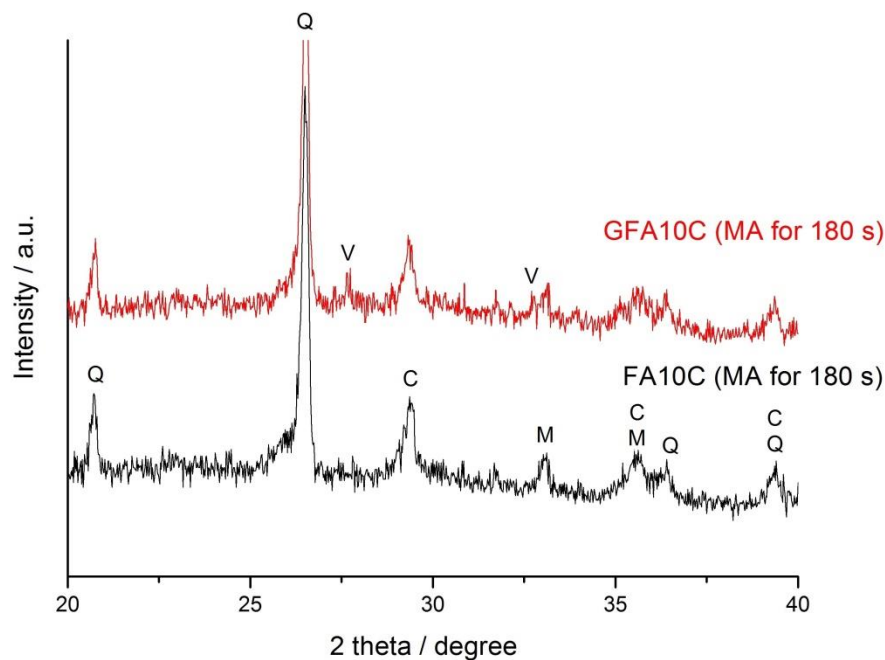

Figure 11. The X-ray diffraction patterns of the blend containing 10% $CaCO_3$ (FA10C) milled for 180 s and of the geopolymer prepared using this blend after 28 d of curing (GFA10C). Phases marked are: Q—quartz, M—mullite, C—calcite, V—vaterite.

One can expect that vaterite is also formed in the pastes with lower calcite content, but its amount is probably below the detection limit by XRD. In particular, the presence of a small amount of vaterite in GFA5C may be evidenced by the shoulder in the DTG curve of this specimen in the temperature range of 480–600 °C (Figure 9). It seems plausible that the formation of vaterite is related to a more complex process and involves interaction of Ca^{2+} ions with Si and Al species in solution until oversaturation with respect to vaterite is reached.

FTIR spectra of the FA and the FA10C blend milled for 180 s, as well as the geopolymers prepared using these raw materials in 28-d age, are presented in Figure 12. The main absorption band at 1090 cm^{-1} is related to the asymmetric stretching Si-O-T (T = Si, Al) vibrations and the band at 460 cm^{-1} is associated with Si-O-T bending vibrations. The IR peaks in the 800–600 cm^{-1} region are due to the presence of quartz and mullite in the FA [80,83,84]. The broad band in the 3700–3100 cm^{-1} region (O-H stretching vibration) and the band at about 1640 cm^{-1} (H-O-H bending vibration) in the spectra of FA0C and FA10C are related to the water adsorbed by the raw materials from air in the course of milling. Bands at 1438 cm^{-1} and 876 cm^{-1} correspond to the asymmetric stretching and out-of-plane bending vibrations of the CO$_3$ group in calcite, respectively [85,86].
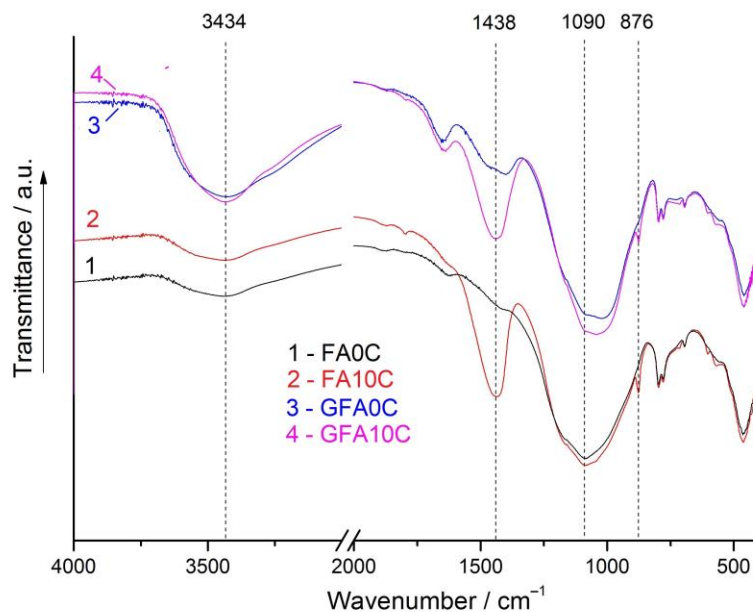

Figure 12. FTIR spectra of the FA (FA0C), the blend containing 10% calcite (FA10C) and the corresponding geopolymers cured for 28 d (GFA0C and GFA10C, respectively). MA of the raw materials was carried out for 180 s.

The main peak associated with the Si-O-T asymmetric stretching vibrations in the spectra of GFA0C and GFA10C appears to be narrower and shifted towards a lower wavenumber (about 1040–1010 cm^{-1}) in comparison to that of the unreacted precursor materials (Figure 12). These changes indicate the formation of a binder product, amorphous sodium-containing aluminosilicate hydrogel (N-A-S-H gel), and can be explained by the substitution of Si for Al in the silicon-oxygen tetrahedra and a decrease in the degree of polymerization of the aluminosilicate framework of the FA [34,80,83,84,87,88]. The geopolymers contain some unreacted FA, which is evidenced by the presence of a shoulder at approximately 1090 cm^{-1} on the main sharp band in their spectra. The intensity of the main peak in the spectrum of GFA10C is obviously higher than of the GFA1C, indicating greater polymerization [39,84]. This observation is consistent with the calorimetric measurements (Figures 6 and 7) and the compressive strength data (Figure 4). The increased intensity of the bands corresponding to OH group vibrations (3434 cm^{-1} and 1640 cm^{-1}) in the spectrum of the GFA10C in comparison to that of the GFA0C can be associated with a larger formation of the reaction product [88], in agreement with the TG results (Figure 8).

The main calcite peak for the GFA10C, at 1438 cm^{-1}, slightly decreased in intensity and broadened compared to that for the FA10C (Figure 12). In line with the XRD (Figure 11) and DTG (Figure 9) data, this is consistent with the partial transformation of calcite to vaterite because in the IR spectrum of vaterite, the main band of the carbonate group is split (1420 and 1490 cm^{-1}) owing to the reduced symmetry of the carbonate ion in the structure of this mineral [86,89]. The broad band in the

1500–1350 cm^{-1} region in the spectrum of GFA0C (Figure 12) is related to the formation of small amounts of sodium carbonates and hydrocarbonates due to the atmospheric carbonation of unreacted alkaline activation media [45,88,90].

3.5. Mössbauer Spectroscopy Analysis

As the FA contains about 9% of iron oxides (Table 1), it is of interest to elucidate if any changes in the iron valence and coordination number occur during the geopolymerization process. The ^{57}Fe Mössbauer spectra of the unblended FA (FA0C), the FA + calcite blend containing 5% calcite (FA5C), mechanically activated for 180 s, and the corresponding geopolymers cured for 28 d are shown as representative examples in Figure 13. The corresponding Mössbauer parameters are tabulated in Table 3.
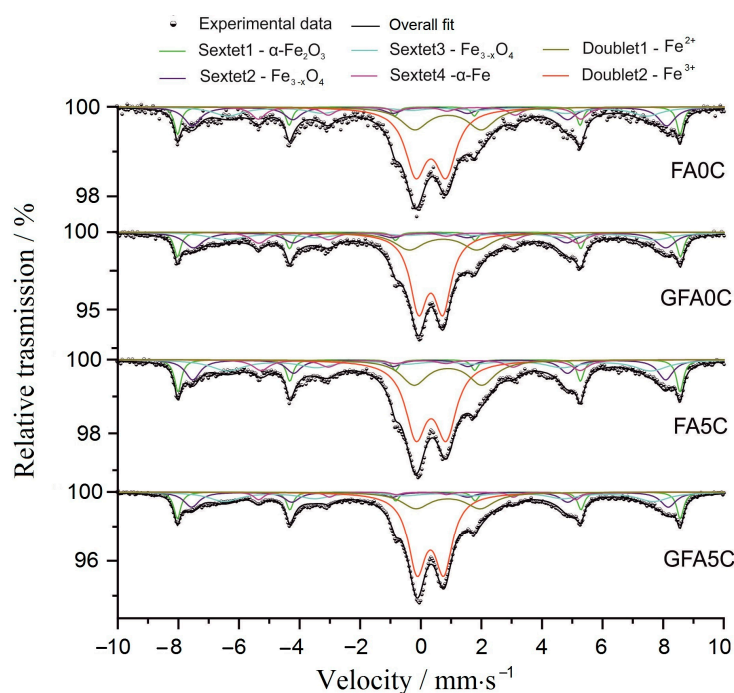

Figure 13. Mössbauer spectra of the FA (FA0C), the FA + calcite blend containing 5% (FA5C), and of the corresponding geopolymers (GFA0C and GFA5C, respectively) cured for 28 d. MA of the raw materials was carried out for 180 s.

The registered Mössbauer spectra were evaluated with a model of four sextets and two doublets. The overall fit is also shown in Figure 13. The parameters of the sextet components indicate the presence of hematite (Sx1), magnetite (Sx2 and Sx3), and metallic iron α-Fe (Sx4). The presence of a small amount of elemental iron in the samples can be explained by the abrasion of the milling bodies during MA. According to the calculated parameters, the registered two doublet components, Db1 and Db2, correspond to octahedrally coordinated iron ions in the third (Fe^{3+}) and second (Fe^{2+}) degree of oxidation, which can be related to their presence in mullite and/or glass phases [91,92]. Comparison of the parameters of the geopolymers (GFA0C and GFA5C) and the precursors (FA0C and FA5C) shows insignificant differences in the environment and the distribution of iron ions in the corresponding phases (Table 3), indicating the relative inertness of iron in geopolymerization. This agrees with the observations of Lloyd et al. [93]. Transformation of the FA to geopolymer as a result of its activation with NaOH solution in the presence of CaCO$_3$ is related to a small increase of the Fe^{3+} component. The small decrease of the isomer shift and quadrupole splitting of the ferric iron for the GFA5C specimen, in comparison to that for the FA5C blend, may indicate the partial reorganization of Fe^{3+} ions after alkali activation by incorporation into the aluminosilicate geopolymer matrix [94]. Iron oxides

with a hyperfine magnetic structure (sextet components) do not undergo significant changes after the formation of the geopolymer.

Table 3. Mössbauer spectral fitting parameters of the FA0C, GFA0C, FA5C and GFA5C specimens (isomer shift IS, quadrupole splitting QS, effective hyperfine magnetic field H_{eff}, linewidth FWHM and relative spectral area G). MA of the raw materials was carried out for 180 s and geopolymers were cured for 28 d.

Sample	Components	IS, mm/s	QS, mm/s	H_{eff}, T	FWHM, mm/s	G, %
FA0C	Sx1-α-Fe$_2$O$_3$	0.36	−0.19	51.4	0.26	10
	Sx2-Fe$_{3-x}$O$_4$	0.30	0.02	48.6	0.66	17
	Sx3-Fe$_{3-x}$O$_4$	0.65	0.01	42.9	1.20	14
	Sx4-α-Fe	0.02	0.01	32.9	0.56	10
	Db1-Fe^{3+}	0.33	0.99	-	0.85	35
	Db2-Fe^{2+}	0.90	2.20	-	1.09	15
GFA0C	Sx1-α-Fe$_2$O$_3$	0.37	−0.20	51.5	0.28	10
	Sx2-Fe$_{3-x}$O$_4$	0.30	0.01	48.3	0.78	17
	Sx3-Fe$_{3-x}$O$_4$	0.65	0.00	43.9	1.47	15
	Sx4-α-Fe	0.02	0.01	32.7	0.66	10
	Db1-Fe^{3+}	0.33	0.80	-	0.68	35
	Db2-Fe^{2+}	0.90	2.24	-	1.16	13
FA5C	Sx1-α-Fe$_2$O$_3$	0.37	−0.20	51.3	0.28	10
	Sx2-Fe$_{3-x}$O$_4$	0.30	0.01	48.4	0.60	14
	Sx3-Fe$_{3-x}$O$_4$	0.61	0.01	43.4	1.36	18
	Sx4-α-Fe	0.00	0.01	32.6	0.45	8
	Db1-Fe^{3+}	0.34	0.99	-	0.84	35
	Db2-Fe^{2+}	0.90	2.24	-	1.05	15
GFA5C	Sx1-α-Fe$_2$O$_3$	0.37	−0.22	51.5	0.28	11
	Sx2-Fe$_{3-x}$O$_4$	0.30	0	48.8	0.70	14
	Sx3-Fe$_{3-x}$O$_4$	0.63	0	43.9	1.27	17
	Sx4-α-Fe	0.02	0.01	32.5	0.41	5
	Db1-Fe^{3+}	0.32	0.88	-	0.68	40
	Db2-Fe^{2+}	0.90	2.12	-	1.13	13

Sx—sextet; Db—doublet.

3.6. Microstructural Studies

The microstructures of selected geopolymer specimens prepared using the raw materials milled for 180 s and cured for 28 d are shown in Figure 14. In comparison to the GFA0C geopolymer based on the 100% FA (Figure 14a), the geopolymers synthesized using blends (GFA5C, Figure 14b, and GFA10C, Figure 14c) are characterized by a more uniform dense microstructure. This can be explained by the higher reactivity of the precursors and by the formation of a greater amount of geopolymer gel in agreement with the strength data (Figure 5). For the elucidation of the role of calcite in the studied binders, the distribution of calcium within the pastes is of great importance. EDS elemental mapping of the GFA1C, GFA3C, and GFA5C specimens (data not shown) indicated a relatively homogeneous distribution of Ca in the form of fine calcite particles embedded in the geopolymer matrix. No newly formed discrete high calcium phases in the binder structure of these specimens were detected within the resolution of the used SEM/EDS analysis. By contrast, this was not the case for the geopolymer based on the blend containing 10% calcite (GFA10C).
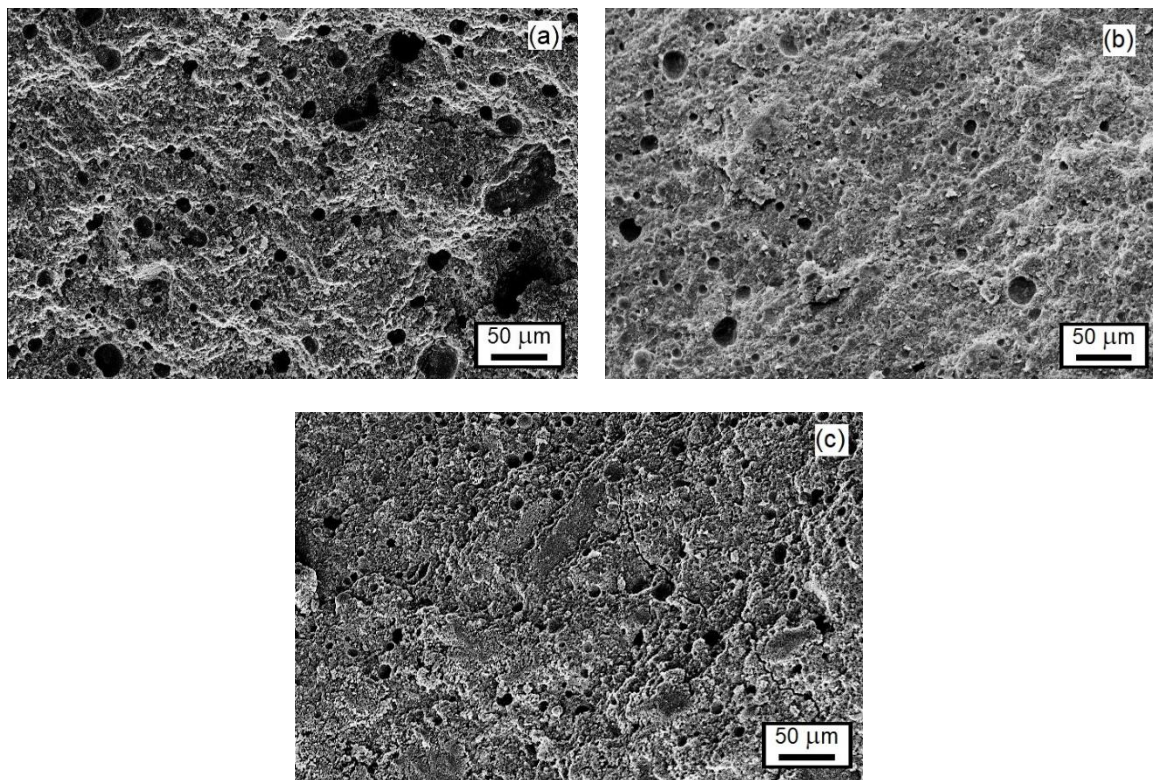
Figure 14. SEM images of the geopolymers cured for 28 d: GFA0C (**a**), GFA5C (**b**) and GFA10C (**c**). MA of the raw materials was carried out for 180 s.

Figure 15 shows the magnified SEM image of the GFA10C specimen cured for 28 days. The particles of unreacted raw material covered with the gel, and closed spherical pores, are clearly seen within the paste microstructure. The spherical pores are likely formed as a result of the entrapment of air during the paste preparation. Within the geopolymer gel (the upper right corner in the Figure 15), particles of a newly formed phase can be seen. This phase was identified by EDS analysis as $Ca(OH)_2$. The formation of small amounts of calcium hydroxide, which could not be detected in the sample by X-ray diffraction and FTIR spectroscopy, most probably occurs through the dissolution of calcite in the NaOH solution followed by precipitation of $Ca(OH)_2$ [95]. This result is in line with observations of Provis et al. [96]. Using high-resolution synchrotron X-ray fluorescence, they revealed that discrete calcium hydroxide regions, a few tens of nanometers in size (not detectable by XRD), were scattered throughout the geopolymer binder synthesized by hydroxide (KOH) activation of low-calcium fly ash. Therefore, $Ca(OH)_2$ can also be formed in small amounts in the geopolymers with a lower content of calcite (GFA0C-GFA5C). It should also be noted that calcium hydroxide precipitates of size about 10 μm, which were also not identified by X-ray diffraction, were observed by SEM-EDS in the microstructure of geopolymers prepared by activation of the 80% metakaolin + 20% calcite blend with sodium silicate solution [60].

Thus, in the studied geopolymer binders, calcite, obviously, is not only a micro aggregate, but also an active component which affects the geopolymerization reactions and the mechanical properties of the final geopolymers. Particularly, on the one hand, the precipitation of small amounts of $Ca(OH)_2$, as a result of calcite dissolution, decreases the pH of NaOH solution and, consequently, may decrease, to some extent, the dissolution rate of the FA and further precipitation of the N-A-S-H gel [95]. However, on the other hand, both calcite and newly formed Ca-containing phases (vaterite and calcium hydroxide) provide nucleation sites with the ability to accelerate sodium-containing aluminosilicate hydrogel formation [95,97], which is in agreement with the calorimetric (Figures 6 and 7), thermogravimetric (Figure 8), FTIR spectroscopy (Figure 12), and strength (Figures 4 and 5) data.
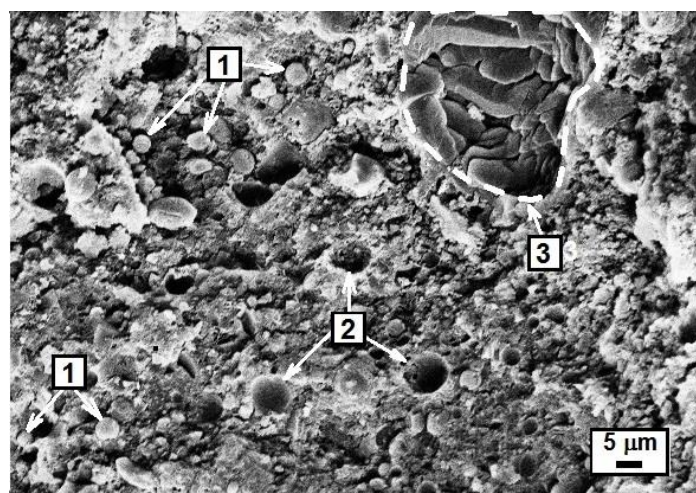
Figure 15. Magnified SEM image of the GFA10C geopolymer cured for 28 days (MA of the FA10C blend was carried out for 180 s): (1)—particles of the partially reacted FA covered with the gel; (2)—closed spherical pores; (3)—Ca(OH)$_2$.

4. Conclusions

The geopolymers based on the mechanically activated FA with the addition of natural calcite were synthesized using sodium hydroxide solution. Processes occurring in the course of MA of the blends, and their activation with sodium hydroxide solution, were investigated in relation to the strength of the geopolymers.

The key findings from this study include the following:

1. MA of the FA + calcite blends in a planetary mill resulted in a considerably larger mineral lattice disordering, and/or decrease of crystallite size, of calcite in comparison to those of quartz and mullite present in the FA, which can be explained by the difference in hardness of the minerals.
2. With an increase of calcite percentage (up to 10%) in the blend and the MA time, the compressive strength of the geopolymers tended to increase, which agrees with the isothermal conduction calorimetry results and thermogravimetric, FTIR spectroscopy, and SEM microstructure data. The optimal time of MA was found to be 180 s. The beneficial influence of the calcite addition to the FA on the geopolymer strength was more apparent at an early age of curing.
3. The main geopolymerization product of the mechanically activated (FA + calcite) blends was X-ray amorphous N-A-S-H gel. No new crystalline peaks in the diffractograms of the geopolymers prepared using blends containing 5% calcite or less were revealed. For the geopolymer based on the blend containing 10% calcite, the partial transformation of calcite to vaterite and calcium hydroxide was observed by X-ray diffraction and SEM/EDS, respectively.
4. Only small changes in the Fe valence and coordination number due to geopolymerization were revealed using Mössbauer spectroscopy analysis. This indicates the inertness of iron in the studied geopolymer synthesis.
5. The increase in the strength of the geopolymer due to the addition of calcite to the FA can be explained not only by the effect of the microfiller. Calcite particles, as well as newly formed vaterite and calcium hydroxide, are the centers of the formation of the sodium containing aluminosilicate hydrate gel—the main cementing phase of the geopolymer. The use of MA increases the reactivity of the ash with respect to the alkaline agent, and also leads to a decrease in the size of calcite particles and an increase in their surface area, which accelerates the gelation process.
6. The presented results can be used for further study to prepare high performance geopolymers based on mechanically activated (FA + calcite) blends using alternative types of mills, calcite dosage, alkali agents and curing conditions.

References

1. Gollakota, A.R.K.; Volli, V.; Shu, C.-M. Progressive utilisation prospects of coal fly ash: A review. *Sci. Total Environ.* **2019**, *672*, 951–989. [CrossRef]

2. Yadav, S.; Mondal, S.S. A complete review based on various aspects of pulverized coal combustion. *Int. J. Energy Res.* **2019**, *43*, 3134–3165. [CrossRef]

3. Yao, Z.T.; Ji, X.S.; Sarker, P.K.; Tang, J.H.; Ge, L.Q.; Xia, M.S.; Xi, Y.Q. A comprehensive review on the applications of coal fly ash. *Earth Sci. Rev.* **2015**, *141*, 105–121. [CrossRef]

4. Jayaranjan, M.L.D.; Hullebusch, E.D.; Annachhatre, A.P. Reuse options for coal fired power plant bottom ash and fly ash. *Rev. Environ. Sci. Biotechnol.* **2014**, *13*, 467–486. [CrossRef]

5. Wang, N.; Sun, X.; Zhao, Q.; Yang, Y.; Wang, P. Leachability and adverse effects of coal fly ash: A review. *J. Hazard. Mater.* **2020**, *396*, 122725. [CrossRef]

6. Davidovits, J. *Geopolymer Chemistry and Applications*, 5th ed.; Institut Géopolymère: Saint-Quentin, France, 2020; pp. 23–208.

7. Provis, J.L.; Duxson, P.; Kavalerova, E.; Krivenko, P.V.; Pan, Z.; Puertas, F.; van Deventer, J.S.J. Historical aspects and overview. In *Alkali-Activated Materials: State of the Art Report of RILEM TC 224-AAM*; Provis, J.L., van Deventer, J.S.J., Eds.; Springer Science & Business Media: Dordrecht, The Netherlands, 2014; pp. 11–58.

8. Singh, N.B.; Middendor, B. Geopolymers as an alternative to Portland cement: An overview. *Constr. Build. Mater.* **2020**, *237*, 117455. [CrossRef]

9. Palomo, A.; Krivenko, P.; Garcia-Lodeiro, I.; Kavalerova, E.; Maltseva, O.; Fernández-Jiménez, A. A review on alkaline activation: New analytical perspectives. *Mater. Construcción* **2014**, *64*, e022. [CrossRef]

10. Provis, J.L. Alkali-activated materials. *Cem. Concr. Res.* **2018**, *114*, 40–48. [CrossRef]

11. Rivera, O.G.; Long, W.R.; Weiss, C.A., Jr.; Moser, R.D.; Williams, B.A.; Torres-Cancel, K.; Gore, E.R.; Allison, P.G. Effect of elevated temperature on alkali-activated geopolymeric binders compared to Portland cement-based binders. *Cem. Concr. Res.* **2016**, *90*, 43–51. [CrossRef]

12. Lahoti, M.; Tan, K.H.; Yang, E.-H. A critical review of geopolymer properties for structural fire-resistance applications. *Constr. Build. Mater.* **2019**, *221*, 514–526. [CrossRef]

13. Palomo, A.; Blanco-Varela, M.T.; Granizo, M.L.; Puertas, F.; Vazquez, T.; Grutzeck, M.W. Chemical stability of cementitious materials based on metakaolin. *Cem. Concr. Res.* **1999**, *29*, 997–1004. [CrossRef]

14. Aliques-Granero, J.; Tognonvi, M.T.; Tagnit-Hamoua, A. Durability study of AAMs: Sulfate attack resistance. *Constr. Build. Mater.* **2019**, *229*, 117100. [CrossRef]

15. Deng, N.; An, H.; Cui, H.; Pan, Y.; Wang, B.; Mao, L.; Zhai, J. Effects of gamma-ray irradiation on leaching of simulated ^{133}Cs+ radionuclides from geopolymer wasteforms. *J. Nucl. Mater.* **2015**, *459*, 270–275. [CrossRef]

16. Skorina, T. Ion exchange in amorphous alkali-activated aluminosilicates: Potassium based geopolymers. *Appl. Clay Sci.* **2014**, *87*, 205–211. [CrossRef]

17. O'Connor, S.J.; MacKenzie, K.J.D.; Smith, M.E.; Hanna, J.V. Ion exchange in the charge-balancing sites of aluminosilicate inorganic polymers. *J. Mater. Chem.* **2010**, *20*, 10234–10240. [CrossRef]

18. Shi, C.; Qu, B.; Provis, J.L. Recent progress in low-carbon binders. *Cem. Concr. Res.* **2019**, *122*, 227–250. [CrossRef]

19. Komljenović, M.; Tanasijević, G.; Džunuzović, N.; Provis, J.L. Immobilization of cesium with alkali-activated blast furnace slag. *J. Hazard. Mater.* **2020**, *388*, 121765. [CrossRef]

20. Wu, Y.; Lu, B.; Bai, T.; Wang, H.; Du, F.; Zhang, Y.; Cai, L.; Jiang, C.; Wang, W. Geopolymer, green alkali activated cementitious material: Synthesis, applications and challenges. *Constr. Build. Mater.* **2019**, *224*, 930–949. [CrossRef]

21. Luukkonen, T.; Heponiemi, A.; Runtti, H.; Pesonen, J.; Yliniemi, J.; Lassi, U. Application of alkali-activated materials for water and wastewater treatment: A review. *Rev. Environ. Sci. Biotechnol.* **2019**, *18*, 271–297. [CrossRef]

22. Tang, Z.; Li, W.; Hu, Y.; Zhou, J.L.; Tam, V.W.Y. Review on designs and properties of multifunctional alkali-activated materials (AAMs). *Constr. Build. Mater.* **2019**, *200*, 474–489. [CrossRef]

23. Komnitsas, K.; Zaharaki, D. Geopolymerisation: A review and prospect for the mineral industry. *Miner. Eng.* **2007**, *20*, 1261–1277. [CrossRef]

24. Fernandez-Jimenez, A.; Palomo, A. Characterization of fly ashes, potential reactivity as alkaline cements. *Fuel* **2003**, *82*, 2259–2265. [CrossRef]

25. Duxson, P.; Fernández-Jiménez, A.; Provis, J.L.; Lukey, G.C.; Palomo, A.; van Deventer, J.S.J. Geopolymer technology: The current state of the art. *J. Mater. Sci.* **2007**, *42*, 2917–2933. [CrossRef]

26. Provis, J.L.; Fernández-Jiménez, A.; Kamseu, E.; Leonelli, C.; Palomo, A. Binder chemistry—Low-calcium alkali-activated materials. In *Alkali-Activated Materials: State of the Art Report of RILEM TC 224-AAM*; Provis, J.L., van Deventer, J.S.J., Eds.; Springer Science & Business Media: Dordrecht, The Netherlands, 2014; pp. 93–123.

27. Zhuang, X.Y.; Chen, L.; Komarneni, S.; Zhou, C.H.; Tong, D.S.; Yang, H.M.; Yu, W.H.; Wang, H. Fly ash-based geopolymer: Clean production, properties and applications. *J. Clean. Prod.* **2016**, *125*, 253–267. [CrossRef]

28. Fernandez-Jimenez, A.; García-Lodeiro, I.; Palomo, A. Durability of alkali-activated fly ash cementitious materials. *J. Mater. Sci.* **2007**, *42*, 3055–3065. [CrossRef]

29. Kumar, R.; Kumar, S.; Mehrotra, S.P. Towards sustainable solutions for fly ash through mechanical activation. *Resourc. Conserv. Recyc.* **2007**, *52*, 157–179. [CrossRef]

30. Rickard, W.D.A.; Williams, R.; Temuujin, J.; van Riessen, A. Assessing the suitability of three Australian fly ashes as an aluminosilicate source for geopolymers in high temperature applications. *Mater. Sci. Eng. A.* **2011**, *528*, 3390–3397. [CrossRef]

31. Cristelo, N.; Tavares, P.; Lucas, E.; Miranda, T.; Oliveira, D. Quantitative and qualitative assessment of the amorphous phase of a Class F fly ash dissolved during alkali activation reactions—Effect of mechanical activation, solution concentration and temperature. *Compos. Part. B Eng.* **2016**, *103*, 1–14. [CrossRef]

32. Kumar, R.; Kumar, S.; Alex, T.C.; Singla, R. Mapping of calorimetric response for the geopolymerisation of mechanically activated fly ash. *J. Therm. Anal. Calorim.* **2019**, *136*, 1117–1133. [CrossRef]

33. Nath, S.K.; Kumar, S. Reaction kinetics of fly ash geopolymerization: Role of particle size controlled by using ball mill. *Adv. Powder Technol.* **2019**, *30*, 1079–1088. [CrossRef]

34. Rees, C.A.; Provis, J.L.; Lukey, G.C.; van Deventer, J.S.J. In situ ATR-FTIR study of the early stages of fly ash geopolymer gel formation. *Langmuir* **2007**, *23*, 9076–9082. [CrossRef] [PubMed]

35. Zhang, Z.; Provis, J.L.; Zou, J.; Reid, A.; Wang, H. Toward an indexing approach to evaluate fly ashes for geopolymer manufacture. *Cem. Concr. Res.* **2016**, *85*, 163–173. [CrossRef]

36. Shekhovtsova, J.; Zhernovsky, I.; Kovtun, M.; Kozhukhova, N.; Zhernovskaya, I.; Kearsley, E. Estimation of fly ash reactivity for use in alkali-activated cements—A step towards sustainable building material and waste utilization. *J. Clean. Prod.* **2018**, *178*, 22–33. [CrossRef]

37. Sanalkumar, K.U.A.; Lahoti, M.; Yang, E.H. Investigating the potential reactivity of fly ash for geopolymerization. *Constr. Build. Mater.* **2019**, *225*, 283–291. [CrossRef]

38. Kumar, S.; Kumar, R.; Alex, T.C.; Bandopadhyay, A.; Mehrotra, S.P. Influence of reactivity of fly ash on geopolymerisation. *Adv. Appl. Ceram.* **2007**, *106*, 120–127. [CrossRef]

39. Kumar, S.; Kumar, R. Mechanical activation of fly ash: Effect on reaction, structure and properties of resulting geopolymer. *Ceram. Int.* **2011**, *37*, 533–541. [CrossRef]

40. Mucsi, G.; Molnar, Z.; Kumar, S. Geopolymerisation of mechanically activated lignite and brown coal fly ash. *Acta Phys. Pol. A.* **2014**, *126*, 994–998. [CrossRef]

41. Matsuoka, M.; Yokoyama, K.; Okura, K.; Murayama, N.; Ueda, M.; Naito, M. Synthesis of geopolymers from mechanically activated coal fly ash and improvement of their mechanical properties. *Minerals* **2019**, *9*, 791. [CrossRef]

42. Temuujin, J.; Williams, R.P.; van Riessen, A. Effect of mechanical activation of fly ash on the properties of geopolymer cured at ambient temperature. *J. Mater. Process. Technol.* **2009**, *209*, 5276–5280. [CrossRef]

43. Chu, Y.-S.; Davaabal, B.; Kim, D.-S.; Seo, S.-K.; Kim, Y.; Ruescher, C.; Temuujin, J. Reactivity of fly ashes milled in different milling devices. *Rev. Adv. Mater. Sci.* **2019**, *58*, 179–188. [CrossRef]

44. Mucsi, G.; Kumar, S.; Csoke, B.; Kumar, R.; Molnar, Z.; Racz, A.; Mádai, F.; Debreczeni, Á. Control of geopolymer properties by grinding of land filled fly ash. *Int. J. Min. Proc.* **2015**, *143*, 50–58. [CrossRef]

45. Kumar, S.; Mucsi, G.; Kristály, F.; Pekker, P. Mechanical activation of fly ash and its influence on micro and nano-structural behaviour of resulting geopolymers. *Adv. Powder Technol.* **2017**, *28*, 805–813. [CrossRef]

46. Marjanovic, N.; Komljenovic, M.; Bascarevic, Z.; Nikolic, V. Improving reactivity of fly ash and properties of ensuing geopolymers through mechanical activation. *Constr. Build. Mater.* **2014**, *57*, 151–162. [CrossRef]

47. Kato, K.; Xin, Y.; Hitomi, T.; Shirai, T. Surface modification of fly ash by mechano-chemical treatment. *Ceram. Int.* **2019**, *45*, 849–853. [CrossRef]

48. Fernández-Jiménez, A.; Garcia-Lodeiro, I.; Maltseva, O.; Palomo, A. Mechanical-chemical activation of coal fly ashes: An effective way for recycling and make cementitious materials. *Front. Mater.* **2019**, *6*, 51. [CrossRef]

49. Mucsi, G. Mechanical activation of power station fly ash by grinding: A review. *J. Silic. Based Compos. Mater.* **2016**, *68*, 56–61. [CrossRef]

50. Boldyrev, V.V. Mechanochemistry and mechanical activation of solids. *Russ. Chem. Rev.* **2006**, *75*, 177–189. [CrossRef]

51. Butyagin, P.Y. Problems in mechanochemistry and prospects for its development. *Russ. Chem. Rev.* **1994**, *63*, 965–976. [CrossRef]

52. Baláž, P.; Achimovičová, M.; Baláž, M.; Billik, P.; Cherkezova-Zheleva, Z.; Criado, J.M.; Delogu, F.; Dutková, E.; Gaffet, E.; Gotor, F.H.; et al. Hallmarks of mechanochemistry: From nanoparticles to technology. *Chem. Soc. Rev.* **2013**, *42*, 7571–7637. [CrossRef]

53. Avvakumov, E.G. *Mechanical Methods for Activation of Chemical Processes*; Nauka: Novosibirsk, Russia, 1986; p. 305. (In Russian)

54. Juhasz, Z.; Opoczky, L. *Mechanical Activation of Minerals by Grinding: Pulverizing and Morphology of Particles*; Ellis Horwood Ltd.: Chichester, UK, 1990; p. 234.

55. Alghamdi, H.; Nair, S.A.; Neithalath, N. Insights into material design, extrusion rheology, and properties of 3D-printable alkali-activated fly ash-based binders. *Mater. Design* **2019**, *167*, 107634. [CrossRef]

56. Mermerdaş, K.; Manguri, S.; Nassani, D.E.; Oleiwi, S.M. Effect of aggregate properties on the mechanical and absorption characteristics of geopolymer mortar. *Eng. Sci. Technol. Int. J.* **2017**, *20*, 1642–1652. [CrossRef]

57. Embong, R.; Kusbiantoro, A.; Shafiq, N.; Nuruddin, M.F. Strength and microstructural properties of fly ash based geopolymer concrete containing high-calcium and water-absorptive aggregate. *J. Clean. Prod.* **2016**, *112*, 816–822. [CrossRef]

58. Azimi, E.A.; Abdullah, M.M.A.B.; Vizureanu, P.; Salleh, M.A.A.M.; Sandu, A.V.; Chaiprapa, J.; Yoriya, S.; Hussin, K.; Aziz, I.H. Strength development and elemental distribution of dolomite/fly ash geopolymer composite under elevated temperature. *Materials* **2020**, *13*, 1015. [CrossRef] [PubMed]

59. Aboulayt, A.; Riahi, M.; Touhami, M.O.; Hannache, H.; Gomina, M.; Moussa, R. Properties of metakaolin based geopolymer incorporating calcium carbonate. *Adv. Powder Technol.* **2017**, *28*, 2393–2401. [CrossRef]

60. Yip, C.; Provis, J.; Lukey, G.; van Deventer, J. Carbonate mineral addition to metakaolin-based geopolymers. *Cem. Concr. Compos.* **2008**, *30*, 979–985. [CrossRef]

61. Qian, J.; Song, M. Study on influence of limestone powder on the fresh and hardened properties of early age metakaolin based geopolymer. In *Calcined Clays for Sustainable Concrete*; Scrivener, K., Favier, A., Eds.; RILEM Book Series; Springer: Lausanne, Switzerland, 2015; Volume 10, pp. 253–259. [CrossRef]

62. Cwirzen, A.; Provis, J.L.; Penttala, V.; Habermehl-Cwirzen, K. The effect of limestone on sodium hydroxide-activated metakaolin-based geopolymers. *Constr. Build. Mater.* **2014**, *66*, 53–62. [CrossRef]

63. Perez-Cortes, P.; Escalante-Garcia, J.I. Alkali activated metakaolin with high limestone contents—Statistical modeling of strength and environmental and cost analyses. *Cem. Concr. Compos.* **2020**, *106*, 103450. [CrossRef]

64. Bayiha, B.N.; Billong, N.; Yamb, E.; Kaze, R.C.; Nzengwa, R. Effect of limestone dosages on some properties of geopolymer from thermally activated halloysite. *Constr. Build. Mater.* **2019**, *217*, 28–35. [CrossRef]

65. Rakhimova, N.; Rakhimov, R.; Morozov, V.; Gaifullin, A.R.; Potapova, L.; Gubaidullina, A.M.; Osin, Y.N. Marl-based geopolymers incorporated with limestone: A feasibility study. *J. Cryst. Solids* **2018**, *492*, 1–10. [CrossRef]

66. Ortega-Zavala, D.E.; Santana-Carrillo, J.L.; Burciaga-Díaz, O.; García, J.I.E. An initial study on alkali activated limestone binders. *Cem. Concr. Res.* **2019**, *120*, 267–278. [CrossRef]

67. Kalinkin, A.M.; Gurevich, B.I.; Pakhomovskii, Y.A.; Kalinkina, E.V.; Tyukavkina, V.V. Effect of mechanical activation of magnesia-ferriferous slags in CO_2 on their properties. *Russ. J. Appl. Chem.* **2009**, *82*, 1346–1350. [CrossRef]

68. Kalinkina, E.V.; Gurevich, B.I.; Kalinkin, A.M. Alkali-activated binder based on milled antigorite. *Minerals* **2018**, *8*, 503. [CrossRef]

69. Lide, D.R. (Ed.) *CRC Handbook of Chemistry and Physics*, 89th ed.; CRC Press, Taylor and Francis Group: Boca Raton, FL, USA, 2008; p. 2736.

70. Samantasinghar, S.; Singh, S. Effects of curing environment on strength and microstructure of alkali-activated fly ash-slag binder. *Constr. Build. Mater.* **2020**, 117481. [CrossRef]

71. Palomo, A.; Alonso, S.; Fernández-Jiménez, A.; Sobrados, I.; Sanz, J. Alkaline activation of fly ashes: NMR study of the reaction products. *J. Am. Ceram. Soc.* **2004**, *87*, 1141–1145. [CrossRef]

72. Alonso, S.; Palomo, A. Alkaline activation of metakaolin and calcium hydroxide mixtures: Influence of temperature, activator concentration and solids ratio. *Mater. Lett.* **2001**, *47*, 55–62. [CrossRef]

73. Puligilla, S.; Mondal, P. Co-existence of aluminosilicate and calcium silicate gel characterized through selective dissolution and FTIR spectral subtraction. *Cem. Concr. Res.* **2015**, *70*, 39–49. [CrossRef]

74. Chen, X.; Sutrisno, A.; Struble, L.J. Effects of calcium on setting mechanism of metakaolin-based geopolymer. *J. Am. Ceram. Soc.* **2018**, *101*, 957–968. [CrossRef]

75. Gao, X.; Yu, Q.L.; Brouwers, H.J.H. Properties of alkali activated slag-fly ash blends with limestone addition. *Cem. Concr. Compos.* **2015**, *59*, 119–128. [CrossRef]

76. Puligilla, S.; Mondal, P. Role of slag in microstructural development and hardening of fly ash-slag geopolymer. *Cem. Concr. Res.* **2013**, *43*, 70–80. [CrossRef]

77. Duxson, P.; Lukey, G.C.; van Deventer, J.S.J. Physical evolution of Na-geopolymer derived from metakaolin up to 1000 °C. *J. Mater. Sci.* **2007**, *42*, 3044–3054. [CrossRef]

78. Rodríguez, E.D.; Bernal, S.A.; Provis, J.L.; Paya, J.; Monzo, J.M.; Borrachero, M.V. Effect of nanosilica-based activators on the performance of an alkali-activated fly ash binder. *Cem. Concr. Compos.* **2013**, *35*, 1–11. [CrossRef]

79. Bernal, S.A.; Provis, J.L.; Walkley, B.; San Nicolas, R.; Gehman, J.D.; Brice, D.G.; Kilcullen, A.R.; Duxson, P.; van Deventer, J.S.J. Gel nanostructure in alkali-activated binders based on slag and fly ash, and effects of accelerated carbonation. *Cem. Concr. Res.* **2013**, *53*, 127–144. [CrossRef]

80. Lee, W.K.W.; Deventer, J.S.J.V. Use of infrared spectroscopy to study geopolymerization of heterogeneous amorphous aluminosilicates. *Langmuir* **2003**, *19*, 8726–8734. [CrossRef]

81. Navrotsky, A. Energetic clues to pathways to biomineralization: Precursors, clusters, and nanoparticles. *Proc. Natl. Acad. Sci. USA* **2004**, *101*, 12096–12101. [CrossRef] [PubMed]

82. Konno, H.; Nanri, Y.; Kitamura, M. Crystallization of aragonite in the causticizing reaction. *Powder Technol.* **2002**, *123*, 33–39. [CrossRef]

83. Fernandez-Jimenez, A.; Palomo, A. Mid-infrared spectroscopic studies of alkali activated fly ash structure. *Microporous Mesoporous Mater.* **2005**, *86*, 207–214. [CrossRef]

84. Alvarez-Ayuso, E.; Querol, X.; Plana, F.; Alastuey, A.; Moreno, N.; Izquierdo, M.; Font, O.; Moreno, T.; Diez, S.; Vázquez, E.; et al. Environmental, physical and structural characterisation of geopolymer matrixes synthesised from coal (co-) combustion fly ashes. *J. Hazard. Mater.* **2008**, *154*, 175–183. [CrossRef]

85. Nakamoto, K. *Infrared and Raman Spectra of Inorganic and Coordination Compounds: Part A: Theory and Applications in Inorganic Chemistry*, 5th ed.; Wiley: New York, NY, USA, 1997; p. 387.

86. White, W.B. The carbonate minerals. In *The Infrared Spectra of Minerals*; Farmer, W.C., Ed.; Mineralogical Society: London, UK, 1974; pp. 227–284.

87. Nath, S.K.; Maitra, S.; Mukherjee, S.; Kumar, S. Microstructural and morphological evolution of fly ash based geopolymers. *Constr. Build. Mater.* **2016**, *111*, 758–765. [CrossRef]

88. Rozek, P.; Krol, M.; Mozgawa, W. Spectroscopic studies of fly ash-based geopolymers. *Spectrochim. Acta A. Mol. Biomol. Spectrosc.* **2018**, *198*, 283–289. [CrossRef]

89. Sato, M.; Matsuda, S. Structure of vaterite and infrared spectra. *Z. Cristallogr.* **1969**, *129*, 405–410. [CrossRef]

90. Criado, M.; Palomo, A.; Fernandez-Jimenez, A. Alkali activation of fly ashes. Part 1. Effect of curing conditions on the carbonation of the reaction products. *Fuel* **2005**, *84*, 2048–2054. [CrossRef]

91. Zyryanov, V.V.; Petrov, S.A.; Matvienko, A.A. Characterization of spinel and magnetospheres of coal fly ashes collected in power plants in the former USSR. *Fuel* **2011**, *90*, 486–492. [CrossRef]

92. Szumiata, T.; Brzozka, K.; Gorka, B. Iron speciation in coal fly ashes-chemical and Mossbauer analysis. *Hyperfine Interact.* **2014**, *226*, 483–487. [CrossRef]

93. Lloyd, R.R.; Provis, J.L.; van Deventer, J.S.J. Microscopy and microanalysis of inorganic polymer cements. 1: Remnant fly ash particles. *J. Mater. Sci.* **2009**, *44*, 608–619. [CrossRef]

94. Lemougna, P.N.; MacKenzie, K.J.D.; Jameson, G.N.L.; Rahier, H.; Chinje Melo, U.F. The role of iron in the formation of inorganic polymers (geopolymers) from volcanic ash: A ^{57}Fe Mossbauer spectroscopy study. *J. Mater. Sci.* **2013**, *48*, 5280–5286. [CrossRef]

95. Van Deventer, J.S.J.; Provis, J.L.; Duxson, P.; Lukey, G.C. Reaction mechanisms in the geopolymeric conversion of inorganic waste to useful products. *J. Hazard. Mater.* **2007**, *139*, 506–513. [CrossRef]

96. Provis, J.L.; Rose, V.; Bernal, S.A.; van Deventer, J.S.J. High-resolution nanoprobe X-ray fluorescence characterization of heterogeneous calcium and heavy metal distributions in alkali-activated fly ash. *Langmuir* **2009**, *25*, 11897–11904. [CrossRef]

97. Lee, W.K.W.; van Deventer, J.S.J. The effect of ionic contaminants on the early-age properties of alkali-activated fly ash-based cements. *Cem. Conc. Res.* **2002**, *32*, 577–584. [CrossRef]